Sustainable Structures
ISSN: 2789-3111 (Print); ISSN: 2789-312X (Online)
http://www.sustain-dpl.com/journal/sust
DOI: 10.54113/j.sust.2024.000054

***ORIGINAL ARTICLE***

# Structural performance of additive manufactured wood-sodium silicate composite beams for sustainable construction

**Hojat Hematabadi[a], Adefemi A Alade[a], Robert HR Carne[b], Daniel Robertson [b], Milinda Yapa[a], Armando G. McDonald[c], Ahmed A. Ibrahim[a, *]**

[a]Department of Civil and Environmental Engineering, University of Idaho, 83844, Moscow, ID, USA.
[b]Department of Mechanical Engineering, University of Idaho, Moscow, ID, USA.
[c]Department of Forest, Rangeland and Fire Sciences in the College of Natural Resources, University of Idaho, Moscow, ID, USA.
*Corresponding author: Ahmed A. Ibrahim. Email: aibrahim@uidaho.edu

**Abstract:** The current research examines the structural bending performance of additive manufactured wood-sodium silicate composite beams of various span-to-height proportions. Beams consisting of both a single layer as well as two layers of extruded wood-sodium silicate composite were considered. Both groups of beams exhibited a rise in maximum shear force ($V_{max}$), maximum bending moment ($M_{max}$), apparent modulus of elasticity ($MOE_{app}$), and modulus of rupture ($MOR$) when the span-to-height proportions rose. However, the amount of shear stress ($\tau_{max}$) decreased as the span-to-height proportion increased. Furthermore, the flexural and shear stress patterns for span-to-height proportions of 6 and 30 were calculated analytically using the transformed section methodology across the thickness of the beams at different positions of $L/6$, $L/3$, $5L/12$, and $L/2$ of the beam span. The results demonstrated that the bending stress increased as the distances from the supports increased toward the middle of the beam. Compared to single-layer beams, two-layer beams displayed lower stress values overall. In particular, the bending stress was 4.85% lower in the two-layer beam with a span-to-height proportion of 6 than that of the single-layer beams. Furthermore, the single-layer beam's maximum shear stress was slightly greater than the two-layer beams. The greatest shear stress of the single-layer beams were computed 4.27% and 0.46% higher than those of the two-layer beams at span-to-height proportions of 6 and 30, respectively.

**Keywords:** Additive manufacturing; wood-sodium silicate; composite beams; sustainable construction.

## 1 Introduction

Additive manufacturing, or 3D printing, is the method of assembling components from 3D model data by attaching materials, often layer by layer, as specified in the international standard ISO/ASTM 52900. This method offers an alternative to traditional manufacturing techniques, such as molding material or subtracting it through milling [1, 2]. Seven specific types of additive manufacturing methods are material extrusion, material jetting, binder jetting, powder bed fusion, directed energy deposition, vat photopolymerization, and sheet lamination [3]. In comparison to fluid and powder-based additive manufacturing methods, extrusion-based additive manufacturing offers freedom in design, bigger construction sizes, and more cost-effectiveness, all while producing detailed structures [4]. Extrusion-



Received: 3 June 2024; Received in revised form: 4 August 2024; Accepted: 8 September 2024

based additive manufacturing was initially designed for polymeric filament materials. However, this technology is currently being utilized with an extensive array of other items encompassing, ceramics [5], concretes [6], sands [7], food materials [8], metallics [9], biomaterials [10], composites [11], multi-materials, intelligent materials [12], energetic materials, and glasses [13].

Additive manufacturing has the potential to completely transform the construction sector in several ways. For example, capability to generate intricate geometries and fabricate both structural and architectural features could be particularly useful in renovation [14-16]. The recent advent of 3D printed homes has minimized the need for formwork and human labor, resulting in reduced construction expenses and decreased waste generation when compared to traditional methods [17]. In addition, 3D printed buildings provide enhanced design versatility, enabling the incorporation of complex geometries [18], as well as increased functionality [16]. Additive manufacturing also enables more environmentally friendly and sustainable construction. For example, 3D-printed earthen structures and fully recyclable structures have recently been produced. Significant progress has also been made in 3D printed concrete structures that incorporate composite aggregates, bio-based components and other environmentally friendly polymers and materials [19]. Similarly, recent progress in the science of materials and manufacturing techniques has enabled 3D printed buildings to possess structures and characteristics that are both highly compatible and functional.

The utilization of raw materials in 3D printing in an efficient manner is resulting in the production of low or zero waste [20]. Considerable attention has been devoted to biodegradable additive manufacturing technologies, including the research, creation, and evaluation of recycled and environmentally friendly materials such as wood, cellulose, and lignin [21, 22]. Additionally, fiber, particle, and nanocomposite reinforced wood materials have garnered attention [23]. However, the real-world applications of 3D printed wood can be limited by issues with consistency of material, structural integrity, print accuracy, and environmental impact. The strength, texture, and moisture content of wood-based materials are subject to variation which may have an impact on the dependability and quality of 3D printed items [24]. However, creating cutting-edge wood-based composites with consistent properties and improved mechanical performance may be one way to tackle these issues. The formulation of wood filaments is being optimized by researchers and manufacturers in an effort to minimize defects and achieve consistent extrusion. Furthermore, adding cutting-edge printing methods like multi-axis printing and layer reinforcement can enhance the structural stability and weight-bearing ability of 3D printed wood products.

The possibility of additively manufacturing buildings using wood fibers presents several advantages and is becoming an active area of research [25, 26]. In particular, it has been shown that additive manufacturing of wood composites could significantly reduce carbon emission associated with the construction industry [27]. Wood is an abundant and sustainable material [21] and could therefore significantly reduce the cost 3D printed goods as well. When used in additive manufacturing wood is typically ground to a powder and subsequently combined with adhesives, plastics, gypsum, natural fiber, or cement [28]. Orji et al. [29] and Carne et al. [30] have effectively3D printed wood composites using a sodium silicate binder. Combining the inherent sustainability of wood with the improved mechanical qualities offered by sodium silicate, wood sodium silicate printed timber material creates a composite that is both incredibly resilient and environmentally friendly. Compared to traditional building materials, this material ensures a lower environmental impact by utilizing the renewable nature of wood. A wide range of structural applications can benefit from sodium silicate's enhanced mechanical performance, which includes increased strength, dimensional stability, and fire resistance. Furthermore, because of its compatibility with additive manufacturing techniques, intricate geometries and unique designs can be precisely fabricated, something that is difficult to accomplish with traditional timber processing. Because of its exceptional mechanical qualities, sustainability, and ability to adapt to cutting-edge manufacturing techniques, wood sodium silicate printed timber is seen as a promising material for creative and environmentally friendly building solutions. However, crucial data regarding the mechanical properties, performance, and service capabilities of extrusion printed wood-sodium silicate composites is needed. It is vital to understand the bending behavior of extrusion printed wood-sodium silicate beams to enable their use in structural applications. This study presents data regarding the bending strength of extrusion printed wood-sodium silicate beams manufactured in several different

span-to-height proportions. In the construction industry, knowledge of the structural properties of new printed timber beams can be advantageous for future design.

## 2. Materials and Methodologies

### 2.1. Preparation of materials

Mixed wood species sawmill leftovers were acquired from Plummer Forest Products (Post Falls, USA). Wood flour was obtained by sieving the mill leftovers through a 20-mesh screen followed by a 40-mesh screen. The wood flour had a moisture level of around 8%. On a dry basis, wood flour and a water-based solution of sodium silicate adhesive were combined in a proportion of 50% wood flour to 50% sodium silicate [30].

### 2.2. Specimen manufacturing

The wood flour and aqueous sodium silicate solution were mixed and fed into a single screw extruder at a rate of 47 g/min as described by Carne et al [30]. Two groups of wood-sodium silicate composite beams were printed; the first set consisted of single layer beams with dimensions of 850 mm × 35 ±5 mm × 15 ±2 mm ($L \times W \times T$), the second consisted of two-layer beams with dimensions of 850 mm × 35 ±5 mm × 30 ±2 mm ($L \times W \times T$). After extrusion the beams were placed in an oven at a temperature of 60 ℃ for 60 hours at which point they reached a 12% humidity level as specified by ASTM D 198 standard [31]. Post-drying, the boards were sawn and sanded to definitive measurements of X, Y, Z. The design of the specimens' size in this study was based on recommendations from the ASTM D198 standard, which provide guidelines for investigating the bending properties of wood composite materials in a range of short to long span-to-height proportions to capture the various mechanical behaviors from pure shear to pure bending under variable span bending test. The two-layer beams were sawn thus, the bond line connecting the two layers was positioned at the midpoint of the beam, namely along the neutral bending axis. After sawing and sanding the two-layer and one-layer beams had the same overall width but the two-layer beam was twice as thick. The beams were then placed in a conditioning chamber held at 25 ℃ and 65% relative humidity for two weeks prior to testing. The beams were separated into the five groups shown in **Table 1**.

**Table 1**. Characteristics of extrusion printed wood-sodium silicate beams used in bending tests

| Group | Span-to-height proportion | Width of beams (mm) | Span of single layer beams (mm) | Span of two-layer beams (mm) | Loading Speed (mm/min) |
|---|---|---|---|---|---|
| A | 6:1 | 35 | 60 | 120 | 1 |
| B | 12:1 | 35 | 120 | 240 | 1 |
| C | 18:1 | 35 | 180 | 360 | 1 |
| D | 24:1 | 35 | 240 | 480 | 1 |
| E | 30:1 | 35 | 300 | 600 | 1 |

### 2.3. Bending tests extrusion printed wood-sodium silicate beams

2.3.1. Test arrangements and results

For each group in **Table 1**, a total number of six beams were subjected to a center-point loading test using an INSTRON 5500R-1137 testing machine. The duration of the bending test for each specimen was less than 20 minutes, in accordance with the guidelines described in ASTM D 198 [31]. Each specimens' maximum deflection at the midspan was calculated utilizing a linear variable differential transformer (LVDT). The experimental bending test configuration for small and large span-to-height proportions are depicted in **Fig. 1.**

The maximum shear force ($V_{max}$) and maximum bending moment ($M_{max}$) of beams were measured by Eq. (1) and Eq. (2):

$$V_{max} = \frac{P_{max}}{2} \quad (1)$$

$$M_{max}=\frac{P_{max}*L}{4} \quad (2)$$

where $V_{max}$ presents the upper limit shear force (kN), $M_{max}$ presents the upper limit bending moment (kN-m), $P_{max}$ is the upper limit load (kN) and $L$ is the span length between supports (mm).

The modulus of elasticity ($MOE_{app}$) and the highest bending stress or modulus of rupture ($MOR$) of each specimen was determined by using Eq. (3) and Eq. (4) as standard [31].

$$MOE_{app}=\frac{PL^3}{48I\Delta} \quad (3)$$

$$MOR=\frac{M_{max}}{S} \quad (4)$$

$$S=\frac{2I}{h} \quad (5)$$

$$I=\frac{bh^3}{12} \quad (6)$$

where $P$ presents the applied load within the elastic region of the material (kN), $\Delta$ is displacement at the center of the specimen (mm), $L$ is the span length between supports (mm), $M_{max}$ presents the greatest applied bending moment (kN-m), $S$ presents the section modulus for a rectangular shape ($mm^3$), $I$ is the moment of inertia the specimen's cross-section, $B$ is the width of the beam's sectional area (mm), and $h$ presents the thickness the specimen's sectional area (mm).

The maximum shear stress ($\tau_{max}$) in each specimen was calculated using Eq. (7) which assumes the material is isotropic [32]:

$$\tau_{max}=\frac{3V_{max}}{2A} \quad (7)$$

where $V$ presents the highest transverse shear force under center point bending (kN), and $A$ is the area of the beams cross-section (i.e., b x h).


**Fig. 1.** Center-point loading test of printed timber beams with small span-to-height proportion (left) and large span-to-height proportion (right).

2.3.2. Flexural stiffness and shear stiffness calculations

The effective flexural stiffness ($EI_{eff}$) and the effective shear stiffness ($GA_{eff}$) of test specimens were determined using both the variable span bending test approach (Regression approach) and the simultaneous bending test approach outlined in ASTM D 198 [31].

2.3.2.1. Evaluation of $EI_{eff}$ and $GA_{eff}$ using the regression method

ASTM D198 specifies evaluating a series of beams of differing span lengths to compute the shear modulus ($G$). The modulus of elasticity ($MOE_{app}$) is dependent upon the shear modulus and the true modulus of elasticity ($MOE_{true}$) and can be computed from the load-displacement response of beams of varying span lengths. The apparent modulus of elasticity deflection equation (Eq. 3) is capable of

generating a linear formula of the form y = mx + b by substituting terms. In this equation, y represents the reciprocal of the elasticity modulus, m stands for the reciprocal of the beams' shear modulus, b for the reciprocal of the true elasticity modulus, and x presents a compound of dimensional concepts pertaining to the supports and loaded conditions. These equations follow a similar procedure, but instead of the modulus of elasticity and shear modulus, respectively, they use $EI_{eff}$ and $GA_{eff}$, with the necessary modifications [33–35].

When a beam is loaded in center-point loading both shear deformations and bending deformations are present as shown in equation 9. However, for slender beams (i.e., span-to-height proportion > 10) the bending deformation is much greater than the shear deformation. Consequently, shear deformations are often assumed to be negligible and the second term in Eq. (9) is simply removed. Note that equation 9 can be rearranged to solve for the quantity *EI* which is known as the flexural stiffness of the beam. If shear deformations are not considered when calculating *EI* then we add a subscript specifying this is the apparent flexural stiffness ($EI_{app}$). Whereas if shear deformations are considered then we use a different subscript ($EI_{eff}$) to specify the effective flexural stiffness. Eq. (10) is obtained by rearranging Eq. (9) and eliminating like terms. The terms in Eq. (10) represent the equivalent terms for beams in the y = m*x + b equation mentioned earlier. The y-term represents the reciprocal of apparent flexural stiffness, the m-term represents the reciprocal of shear stiffness, and the b-term represents the reciprocal of flexural stiffness.

$$\Delta_{total}=\frac{PL^3}{48EI_{eff}}+\frac{PL}{4_KGA_{eff}} \tag{9}$$

$$\frac{1}{EI_{app}}=\frac{1}{EI_{eff}}+\frac{1}{GA_{eff}}\left(\frac{12}{kL^2}\right) \tag{10}$$

where $\Delta$ presents the deflection at the center-point of loading, *P* is the load in elastic zone of load-deflection curve, *L* presents the span of the beam under bending (mm), *A* is distance between support and point of loading in center of the beam, $EI_{app}$ is the flexural stiffness at certain span-to-height proportion of the beam (kN-mm$^2$/m), $GA_{eff}$ is the effective shear stiffness of the beam (kN/m), $EI_{eff}$ is the flexural stiffness of the beam (kN-mm$^2$/m), *K* is equal 5/6, the shear coefficient for rectangular sections.

In order to determine the experimental flexural stiffness ($EI_{eff}$) of the beams using a regression approach or the variable span bending test ($EI_{eff,Reg}$), a set of the beams with the specified dimensions reported in **Table 2** were subjected to a center-point loading test at various bending spans. Subsequently, the $EI_{eff,Reg}$ values for these beams were calculated by utilizing the slope of a linear regression estimation within $1/EI_{app}$ and $(12/KL^2)$ in Eq. (9) and Eq. (10) across all spans. Moreover, The $GA_{eff,Reg}$ values of the beams using regression approach were computed from the intercept of a model using linear regression in the reciprocal of the shear rigidity coefficient and the apparent flexural stiffness under center-point bending test in Eq. (9) and Eq. (10).

2.3.2.2. Evaluation of $EI_{eff}$ and $GA_{eff}$ values through simultaneous bending test

The deflection equation's solution is the basis for a simultaneous solution method that is used as an alternative to assess the bending and shear stiffness parameters. Even though this method only uses two spans , it is found to generate results that are equivalent to the ASTM D 198 variable span method [33,34] which utilizes more than two spans. Prior to the introduction of the variable span method in 1992, the simultaneous approach was defined in ASTM D 198.

To calculate the experimental values of simultaneous flexural stiffness ($EI_{eff,Sim}$) and shear ($GA_{eff,Sim}$) for the beams using the methodology of Simultaneous, two spans from the entire dataset reported in **Table 2** were examined. The $EI_{eff,Sim}$ and $GA_{eff,Sim}$ values of the beams were determined through an experimental center-point loading test, using the pure shear values at a span-to-height proportion of 6 and the pure bending values at a span-to-height proportion of 30. Due to the absence of shear deflection and stress in the $EI_{app}$ term during the pure bending test with a span-to-height proportion of 30, $EI_{eff,Sim}$ was calculated using Eq.(3). Moreover, using deflection values obtained from pure shear bending tests for single and two-layer beams at 6 and 12 cm spans, the $GA_{eff,Sim}$ of the beam was computed using Eq. (11) as follows:

$$GA_{\text{eff}}=\frac{1}{\left[\left(\frac{\Delta_{\text{Three Point}}}{P}-\frac{L^3}{48EI_{\text{eff}}}\right)\left(\frac{4K}{L}\right)\right]} \quad (11)$$

where $\Delta$ is the deflection (mm), $P$ is the transmitted force load (N), $L$ is the span (mm), $EI_{\text{eff}}$ is the flexural stiffness (N-mm$^2$/m), $K$ is the (5/6) for the geometry factor for sections that are rectangular.

2.3.3. Analytical flexural and shear stresses distribution of beams

Shear stress distributions in single-layer and two-layer beams were computed using solid mechanics theory in combination with measurements obtained from experimental center-point loading tests at span-to-height proportions of 6 and 30 [32,36].

## 3. Results and discussion

### 3.1. Experimental flexural test

3.1.1. Maximum deflection, maximum shear force and maximum bending moment of beams

The average experimental $\Delta_{\text{pmax}}$, $V_{\text{max}}$, $M_{\text{max}}$ values of single and two-layers the beams calculated using Equations 1-3 are shown in **Table 2**. In both single- and two-layer specimens, with an increase in the span-to-height proportion from 6 to 30, the average $\Delta_{\text{pmax}}$ and $M_{\text{max}}$ values were increased, while the $V_{max}$ values of specimens exhibited a completely opposite trend.

**Table 2**. Average $\Delta_{\text{pmax}}$, $V_{\text{max}}$, $M_{\text{max}}$ values of single- layer and two-layer beams in various span-to-height proportions under bending test.

| | Single layer | | | Two layers | | |
|---|---|---|---|---|---|---|
| Span-to-height proportion | $\Delta_{\text{pmax}}$ (mm) | $V_{\text{max}}$(N) | $M_{\text{max}}$ (kN-m) | $\Delta_{\text{pmax}}$ (mm) | $V_{\text{max}}$(N) | $M_{\text{max}}$(kN-m) |
| 6 | 0.542(±0.04) | 169.3(±12.8) | 5.080(±0.38) | 0.791(±0.1) | 322.7(±39) | 19.3(±2.34) |
| 12 | 0.927(±0.05) | 94.6(±13) | 5.679(±0.78) | 1.869(±0.05) | 165.4(±19.3) | 19.8(±2.32) |
| 18 | 2.027(±0.43) | 66.8(±8.2) | 6.015(±0.73) | 3.865(±0.45) | 116.5(±14.7) | 20.9(±2.64) |
| 24 | 3.362(±0.27) | 50.8(±7.6) | 6.102(±0.91) | 6.941(±0.5) | 96.2(±6.6) | 23.0(±1.5) |
| 30 | 5.085(±0.50) | 41.0 (±2.46) | 6.203(±0.36) | 8.874(±0.42) | 80.0(±4.5) | 24.0(±1.36) |

Based on the experimental results, the lowest and highest averages $\Delta_{\text{pmax}}$ and $M_{\text{max}}$ values for single-layer specimens were 0.54(mm), 5.085 (mm), 5.08 (kN-m) and 6.16 (kN-m), while for the two-layer specimens were 0.79 (mm), 8.874 (mm), 19.36 (kN-m) and 24.02 (kN-m), respectively, at span-to-height proportions 6 and 30. However, the average $V_{\text{max}}$ values of both groups decreased with rising span-to-height proportions from 6 to 30 (**Table 2**). The lowest average $V_{\text{max}}$ values for single- and two-layer beams were 41.06 (N) and 80.08 (N) observed at span-to-height proportion 30, respectively. This behavior of the beams in the process of flexural was comparable to that of solid timber, in which with a rising span-to-height proportion up to 30 subjected to flexural test, the quantity of $V_{\text{max}}$ diminished but the value of deflection and pure bending values in the beam raises [32].

Comparing the average $\Delta_{\text{pmax}}$ and $V_{\text{max}}$ values of single and two-layer groups of beams at span-to-height proportions of 6 and 30, the $\Delta_{\text{pmax}}$ values for two-layer specimens were respectively 31.6% and 42.7% greater than those of single layer ones. While for $V_{max}$ values, these percentages were 47.5% and 48.7% greater respectively. The difference of $\Delta_{\text{pmax}}$ values in each group between single- and two-layer the beams under bending test was due to different spans in which the specimens were tested. More span-to-height proportion wood and wood-based composite beams typically exhibit more midspan deflection in bending tests than shorter beams[32]. Also, the average $V_{max}$ values of two-layer beam specimens were higher than those of the single-layer specimens. This was because they were thicker, which means they could handle more ultimate loading, which led to higher $V_{\text{max}}$ values according to Eq. (1).

The average values of $MOE_{\text{app}}$ and $MOR$ of the beams were calculated using Eq. (3) and Eq. (4). **Fig. 2** and **Fig. 3** show respectively the average $MOE_{\text{app}}$ and $MOR$ values of single-layer and two-layer beams at various span-to-height proportions. As **Fig. 2** and **Fig. 3** indicate, the average $MOE_{\text{app}}$ and $MOR$ was increased with rising span-to-height proportions from 6 to 30. Additionally, both graphs (**Fig.**

**2, Fig. 3**) demonstrate that the rate of increase in $MOE_{app}$ and MOR values was quicker from span to-height proportions of 6 to 18 than from 18 to 30. Furthermore, the results showed that adding layers to the printing process of the beams made a difference in the average $MOE_{app}$ and *MOR* values.

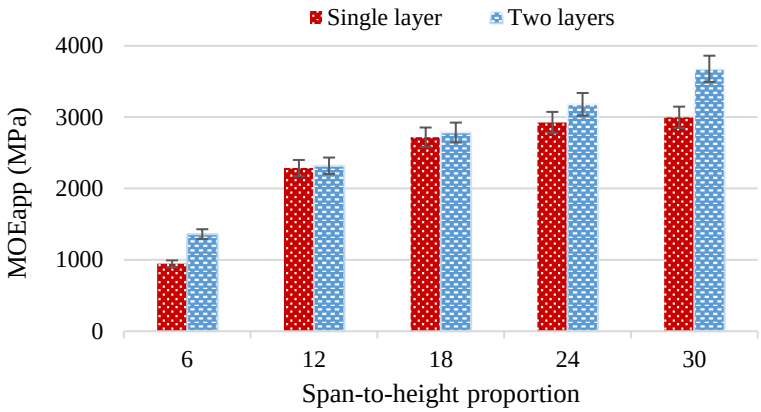


**Fig. 2.** Average apparent modulus of elasticity ($MOE_{app}$) values of both the single-layer and two-layer specimens at various span-to-height proportions.

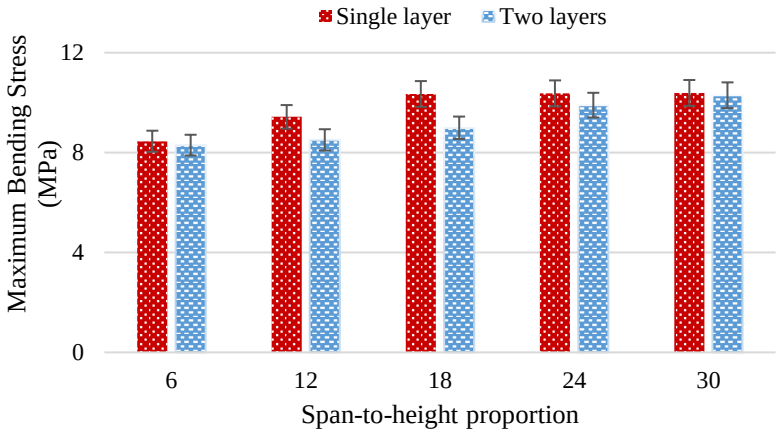


**Fig. 3**. Average modulus of rupture (*MOR*) values of both the single-layer and two-layer specimens at various span-to-height proportions.

3.1.2. Apparent of Elasticity modulus ($MOE_{app}$) and of rupture modulus (*MOR*) of beams

At all span-to-height proportions, the average $MOE_{app}$ values of two-layer beams were greater than those of single-layer beams. The average $MOE_{app}$ values of two-layer beams from span-to-height 6 to 30 were 30.5%, 1.38%, 2.7%, 7.9%, and 18.5% greater than those of single-layer beams, respectively. This difference between the $MOE_{app}$ values of single and two-layer beams may be due to the manufacturing processes of two-layer beams; in fact, at the time of printing the second layer, the extruder nozzle puts pressure on the top of both layers, which makes the two-layer beams somehow stiffer than the single ones. This phenomenon can positively affect the average $MOE_{app}$ values of two-layer beams in different spans.

Conversely, the results specified that the *MOR* values of single-layer beams at all span-to-height proportions from 6 to 30 were greater than those of two-layer ones. When compared to two-layer ones, their *MOR* values were 1.77%, 9.75%, 13.14%, 4.5%, and 0.68% higher, respectively. Two-layer beams had likely had lower MOR values compared to single layer beams because of weak bonding between the layers which led to interlayer delamination. During printing, the second layer was connected to the first layer by a thinner and less wide line of surfaces; consequently, the single-layer beams had an even structure in thickness, which increased their loading capacity.

3.1.3. Maximum Shear Strength ($\tau_{max}$) of beams

An average shear strength of beams ($\tau_{max}$) in each span-to-height proportion was determined by the solid isotropic substances approach based on Eq. 7. The results shown in **Fig. 4** illustrate that $\tau_{max}$ of beams decreases with rising the span-to-height proportion under bending. In fact, the beams with a span-to-height proportion of 6 had the maximum shear stress, and with larger span-to-height proportion, shear stress values decreased. At the maximum difference, the $\tau_{max}$ values for single and two-layer beams, respectively, decreased 75.4% and 75.1% from a span-to-height proportion of 6 to 30. The experimental shear stress values were in line with standard ASTM [31]. For wood and wood composites with a shorter span-to-height proportions of 5 to 6, the deflection of beams at midspan under flexural tests is considered to be pure shear deflection and with rising the span to thickness from 6 to 30, it changes to pure bending deflection. Nevertheless, there was no remarkable difference between the results of $\tau_{max}$ values of single- and two-layer beams in various span-to-height values. The $\tau_{max}$ values of single-layer beams were respectively 1.8%, 9.8%, 13%, 4.6%, and 0.86% higher than those of the two-layer beams. The $\tau_{max}$ values of specimens had an intimate connection with the $V_{max}$ values based on Equation 7. As a result, the decrease of $V_{max}$ values with an altering span-to-height proportion from 6 to 30 reduced $\tau_{max}$ in specimens with a larger span-to-height proportion.

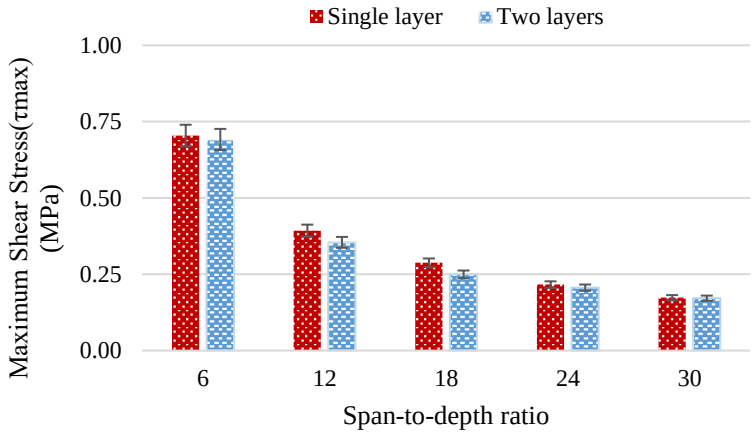


**Fig. 4**. Average maximum shear strength ($\tau_{max}$) values of both single-layer and two-layer specimens at various span-to-height proportions.

### 3.2. Flexural stiffness ($EI_{eff}$) and shear stiffnesses ($GA_{eff}$) of beams

#### 3.2.1. Flexural stiffness ($EI_{eff}$)

The $EI_{eff}$ values of experimental tests ($EI_{eff,Exp}$) of both single and two-layer beams were measured following the regression approach ($EI_{eff,Reg}$) using the slope of linear regression between the terms of $1/EI_{app}$ and $(12/KL^2)$ by formulas (9) and (10), and the simultaneous approach ($EI_{eff,Sim}$) by average experimental results in span-to-height proportion of 30 through Eq. (3), respectively.

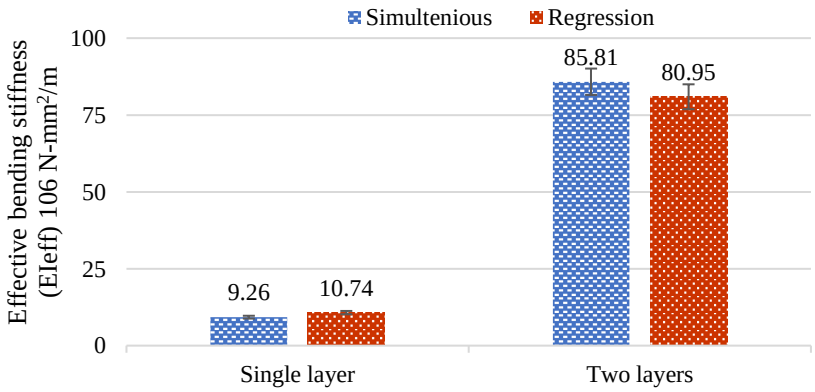


**Fig. 5**. The flexural stiffness ($EI_{eff}$) values of single and two-layer beams based on simultaneous and regression approaches.

**Fig. 5** shows the comparison of the $EI_{eff,Sim}$ and $EI_{eff,Reg}$ values of both groups of the beams. As **Fig. 5** indicates, there was a small difference between the experimental $EI_{eff}$ ($EI_{eff,Exp}$) values of each group of the beams computed in accordance with simultaneous and regression approaches. The methodology of the test and the geometry of the beams can affect the $EI_{eff}$ values of beams. For single-layer beams, $EI_{eff,Reg}$ was calculated to be 13.8% higher than $EI_{eff,Sim.}$ Nonetheless, for the two-layers group, $EI_{eff,Reg}$ was computed to be 6% less than $EI_{eff,Sim}$.

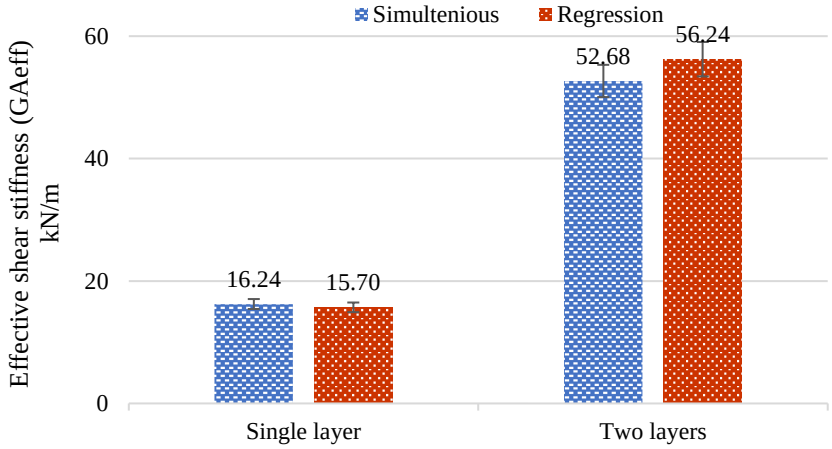


**Fig. 6**. The effective shear stiffness ($GA_{eff}$) values of single and two-layer beams based on simultaneous and regression approaches.

Moreover, the experimental averages of $EI_{eff}$ values of the two-layer specimens were calculated to be 89.2% and 86.7% greater than those of single-layer ones through simultaneous and regression approaches, respectively. The difference between the $EI_{eff,Exp}$ values of single and two-layer beams was due to the different thicknesses of the beams in the two groups. Two-layer specimens had a greater moment of inertia in comparison with single-layer ones, which positively influenced their stiffness.

3.2.2. Effective shear stiffness ($GA_{eff}$)

The $GA_{eff}$ of beams, furthermore, was calculated by the regression approach ($GA_{eff,Reg}$) utilizing Eq. (9) and Eq. (10) to calculate the intercept of a linear regression model within the values $1/EI_{app}$ and (12/KL2), and by the simultaneous approach ($EI_{eff,Sim}$) using Equation 11. The comparison of $GA_{eff,Sim}$ and $GA_{eff,Reg}$ values of both groups of beams is shown in **Fig. 6.** Compared to the $GA_{eff}$ values of two groups of beams, the $GA_{eff}$ values of single-layer beams according to simultaneous (16.2 kN/m) and regression (15.7 kN/m) methods were estimated to be approximately close to each other; however, the average $GA_{eff}$ values by the simultaneous method were estimated to be 3.3% greater. While for two-layer beams, the average $GA_{eff}$ values in accordance with the simultaneous method were estimated to be 6.75% less. Based on the experimental $GA_{eff}$ results, it seems that designing single-layer beams through the regression method is more conservative than simultaneous, whereas for designing two-layer beams, the simultaneous approach computes a discreet $GA_{eff}$ for designing.

### 3.3. Flexural and shear stress of the beams

3.3.1. Bending stress distribution of the beams

In order to assess any differences between the single and two-layer beams under bending, collections of shear stress and bending stress patterns throughout the beams' thickness were evaluated for span-to-height proportions of 6 and 30 at various points of $L/6$, $L/3$, $5L/12$, $L/2$, $7L/12$, $2L/3$, and $5L/6$ of the beam depth. **Fig. 7** shows the single-layer beam at a span-to-height proportion of 6, including the locations of loads and supports, and subsequently a series of bending stress and shear stress patterns across the thickness at the designated places through the specimen's span.

The flexural and shear stress distributions were computed using the transformed section methodology [32,36]. However, in this study, only the flexural and shear stress values of the beam at

7*L*/12, 2*L*/3, and 5*L*/6 were presented since the other points on the right side of the beam were the mirrors of these points.

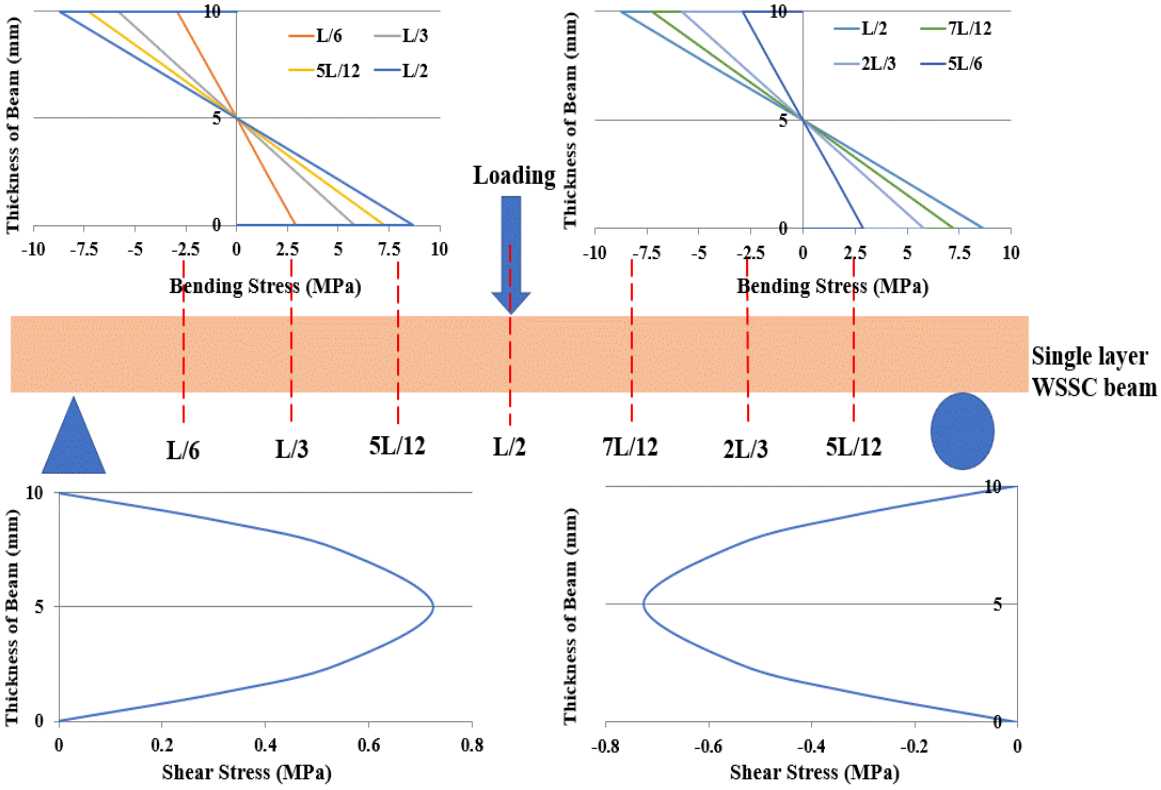


**Fig. 7.** Flexural and shear stress values at the specified points of single-layer beam at span-to-height proportion of 6.

The values of stresses under the flexural test at different sections along the beam span with a span-to-height proportion of 6 are shown in **Fig. 7**, indicating that with rising distances from supports towards the middle of the beam, the bending stress values increase. The bending stress values at *L*/6 and at the middle of the single-layer beam length were about 1.45 MPa and 4.35 MPa, respectively. As is observed from **Fig. 7**, the compressive bending stresses occurred on the top surface of the beam and considered negative stress, while the tension stress happened on the bottom fiber of the beam and was considered as a positive one. In addition to this, the bending stress values at points *L*/6, *L*/3, and 5*L*/12 of the beam were mirrors of 7*L*/12, 2*L*/3, and 5*L*/6.

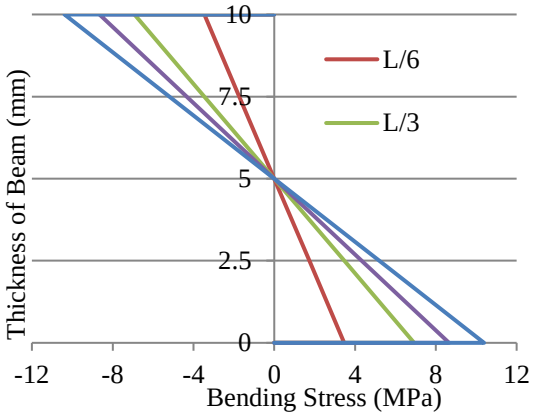


**Fig. 8**. The bending stress values of single-layer beam at span-to-height proportion of 30.

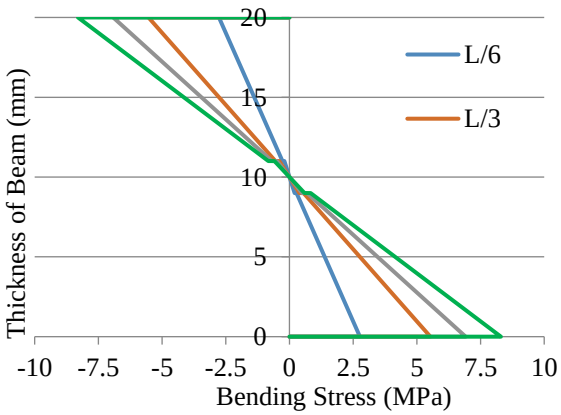


**Fig. 9**. The bending stress values of two-layer beam at span-to-height proportion of 6.

Moreover, the bending stress values for a single-layer beam with a span-to-height proportion of 30 are shown in **Fig. 8**. The graph also indicates that in all points, the bending stress occurred at higher values than those of the beam with a span-to-height proportion of 6. At all points of *L*/6, *L*/3, 5*L*/12,

and *L*/2 of the beam, stress values were approximately 16% greater than those of the beam with a span-to-height proportion of 6. This behavior is not surprising since the longer span beams withstood maximum moment under bending (**Table 2**); thus, the more maximum moment the beam experiences, the more bending stress occurs as compression or tension on top or bottom parts of the beam [32,36].

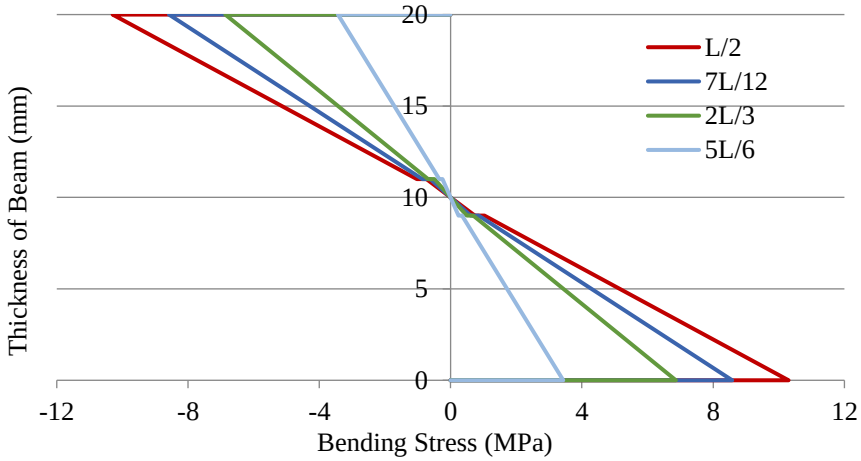


**Fig. 10**. The bending stress values of two-layer beam at span-to-height proportion of 30.

Similarly, the bending stress values for the two-layer beams with both span-to-height proportions of 6 and 30 were the same trend as single-layer beams (**Fig. 9**, **Fig 10**). As for the beam with a span-to-height of 6, the bending stress increased from *L*/6, 0.27 MPa, to its highest rate, 0.83 MPa, at the center of the beam length. In the two-layer beams with a span-to-height proportion of 30, these values were 0.34 MPa at *L*/6 and 1.02 MPa at *L*/2. These were 20.5% and 18.6% higher than the bending stress values for two-layer beams with a span-to-height proportion of 6. Furthermore, comparing the bending stress values for single and two-layer beams, the two-layer beams showed lower values than the single-layer ones. In all points of *L*/6, *L*/3, 5*L*/12, and *L*/2 of two-layer beams with a span-to-height proportion of 6 (**Fig. 9**), the stress was 4.85%, less than that of a single-layer beam (**Fig. 7**). Likewise, at the same point for beams with a span-to-height proportion of 30 (**Fig. 8** and **Fig.10**), this was 0.87% less. As mentioned, the two-layer beams had a lower load bearing capacity in comparison with single-layer beams due to the existence of a weak bonding line between the layers, which made them unequal and different in thickness from single-layer beams.

### 3.3.2. Shear stress distribution of beams

The shear stress values of a single-layer beam with a span-to-height proportion of 6 at points of *L*/6 to 5*L*/12 of span were illustrated in **Fig. 7**. In contrast to bending stress values, shear stress values were calculated to be the same everywhere along the length of the beam. However, the absolute values of stresses from *L*/6 to *L*/2 were the opposite and mirrors of stresses from *L*/2 to 5*L*/2. This behavior was observed since, according to beams mechanics theory, in the center point flexural test, the shear forces were not changed from the support to the middle of the beam. Conversely, in the center point flexural test, the shear stresses happened equally through each beam length [32,36]. The difference between shear stress values at minimum and maximum span-to-height proportions (6 and 30) is shown for single and two-layer beams, respectively, in **Fig. 11** and **Fig. 12**. At the maximum difference, at the center of both beam thicknesses, the shear in a single-layer beam with a span-to-height of 6 was 76.1% greater than that of a beam with a span-to-height of 30 (**Fig. 11**), while for a two-layer beam, this percentage was 75.3% greater (**Fig. 12**).

Additionally, comparing the maximum shear stress values between single and two-layer beams, the maximum shear stress of the single-layer beam was slightly greater than that of the two-layer beam. As at span-to-height of 6 and 30 (**Fig. 11** and **Fig. 12**), the maximum shear stress values of single-layer were 4.27% and 0.46% greater than those of two-layer. This occurred since the single-layer beam had more even features in thickness and could carry more loading under bending than the two-layer beam. Moreover, both graphs (**Fig. 11** and **Fig. 12**) indicate the maximum shear stress distribution occurred at the center of beam thickness, where for two-layer beams there is a bonding line and its strength seems

to be weaker than the other points of beam thickness, while there is no bonding line for single-layer beams and they are more even in thickness.

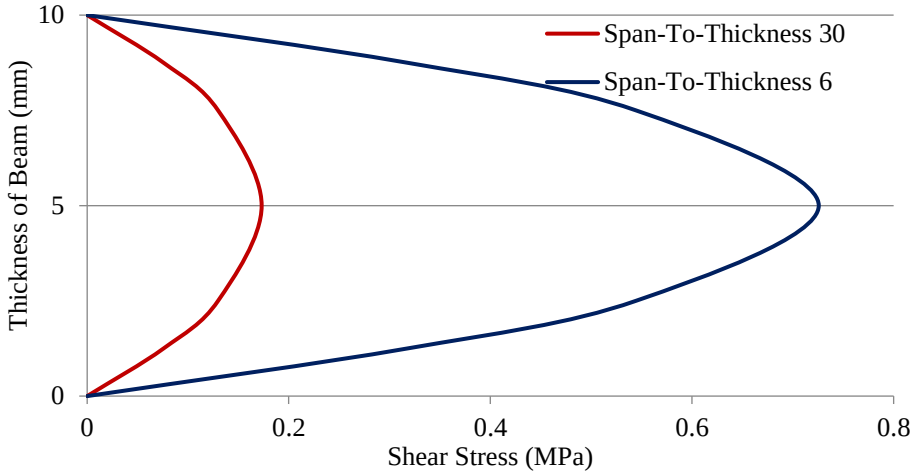


**Fig. 11**. The shear stress values of single-layer beam at span-to-height proportions of 6 and 30.

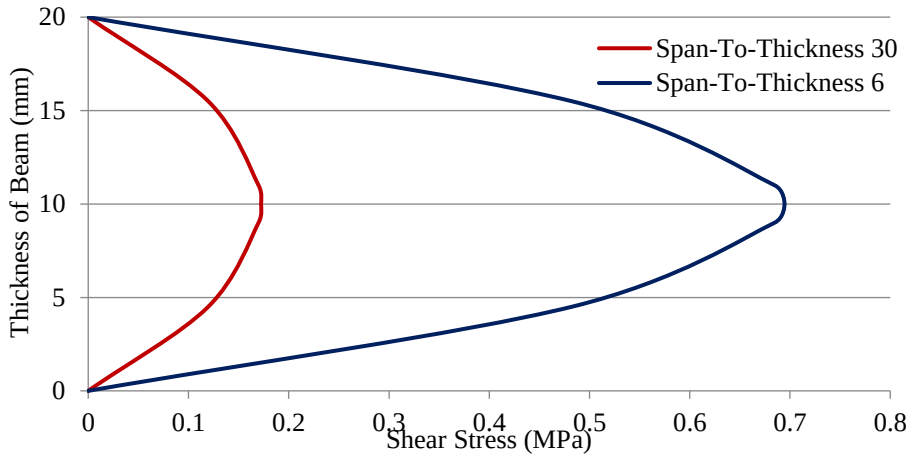


**Fig. 12**. The shear stress values of two-layer beam at span-to-height proportions of 6 and 30.

### 3.4. Failure patterns of the beams

The failure patterns of single-layer and two-layer beams under the center-point loading test are shown in **Fig. 13** and **Fig. 14**, respectively. In all span-to-height proportions, the dominant failure mode of single-layer samples was a tension split at the bottom of the beam at midspan (**Fig. 13**).

This failure pattern was caused by the presence of maximal tensile stresses at the point of greatest bending. Different span-to-height proportions caused varied failure modes of two-layer beams. For example, at a span-to-height proportion of 6 to 18, the failure occurred at the midspan of the beam as a tension split at the bottom layer without any layer delamination. Whereas, the dominant failure modes for two-layer specimens at a span-to-height proportion of 18 to 30 were tension in the bottom layer along with delamination between layers (**Fig. 14**). In fact, with rising the span-to-height proportion, the delamination rate between layers increased as five samples out of the six samples at a span-to-height proportion of 30 were delaminated after starting to crack at the bottom layer. In these beams the initial failure occurred on the bottom layer being loaded in tension. Following this failure the fracture propagated along the length of the beam at the bond line between layers, progressing from the center of the beam to the support points (**Fig. 15**(a) and **Fig. 15** (b)). Only one specimen from the two-layer beams group failed in compression at the top layer followed by delamination between layers (**Fig. 15** (c)). In addition, for one of the two-layer beams with a span-to-height proportion of 24, the initiation of cracks occurred first close to the support, then propagated as delamination towards the center of the beam (**Fig. 15**(d)).

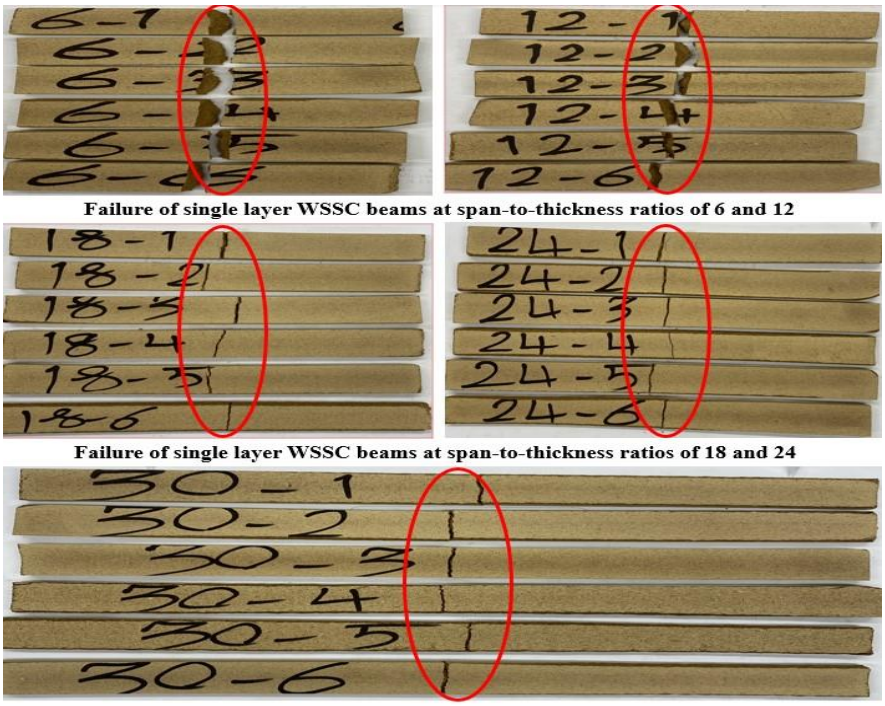


**Fig. 13.** The failure modes of single layer beams in the flexural tests at all span-to-height proportions.


**Fig. 14.** The failure modes of two-layer beams in the flexural tests at all span-to-height proportions.

The failure delamination mode in two-layer specimens with a higher span-to-height proportion is due to the presence of higher bending stress at the bottom layer (**Fig. 8** and **Fig. 10**). In fact, the beams with higher spans tolerated more bending deflection and tension stress under experimental loading than shorter ones under bending loading. When the bottom layer broke under tension, the bottom layer's

response to the fibers breaking apart started a delamination between layers because the bonding line wasn't very strong. This delamination mode then spread from the middle of the beam to the supports. While shorter span beams tolerated smaller bending deflection and less bending stress under experimental loading (**Fig. 9** and **Fig.11**), as a result, the failure in the bottom layer occurred under more shear deflection and stress than bending ones. Consequently, the failure of shorter-span beams happened in the center of the beam without any delamination.

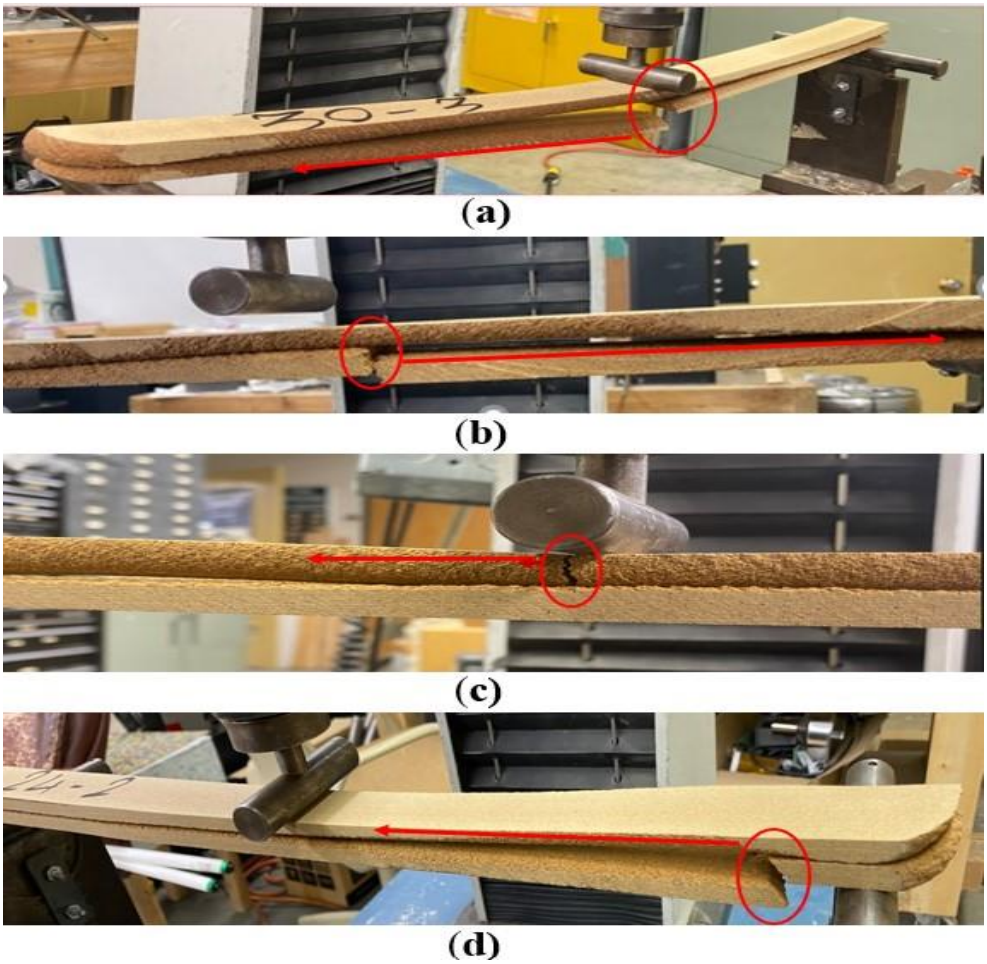


**Fig. 15.** Delamination failure modes of two-layer beams under flexural tests at span at higher span-to-height proportions (24 and 30).

## 4 Conclusions

Using an experimental study and analytical methods, the bending and shear stiffnesses of two groups of single-layer and two-layer extrusion-based additive manufactured timber beams manufactured using wood fiber and sodium silicate were calculated in a range of span-to-height proportions: 6, 12, 18, 24, and 30. The research's findings lead to the following conclusions to be arrived at:

(1) The average $MOE_{app}$ and *MOR* values of both groups of beams was increased as the span-to-height proportion increased between 6 and 30. The mean values of $MOE_{app}$ for two-layer beams were consistently higher than those for single-layer beams across all span-to-height proportions. Conversely, the results indicated that the modulus of rupture (*MOR*) values of single-layer beams were greater than those of two-layer beams across all span-to-height proportions ranging from 6 to 30.

(2) $\tau_{max}$ of beams reduces as the span-to-height proportion increases under bending. The beams with a span-to-height proportion of 6 exhibited the highest shear stress, and the shear values declined as the ratio rose. Nevertheless, no significant distinction was detected between the $\tau_{max}$ values of single- and two-layer beams at varying span-to-height proportion.

(3) For single-layer beams, the $EI_{eff,Reg}$ was found to be 13.8% higher than the $EI_{eff,Sim}$. However, the two-layers beam's $EI_{eff,Reg}$ was found to be 6% less than $EI_{eff,Sim}$. Additionally, it was found that the experimental averages of the $EI_{eff}$ values of the two-layer specimens were, respectively, 86.7% and 89.2% higher than those of the single-layer specimens using regression and simultaneous methods.

(4) The $GA_{eff}$ values of single-layer beams were approximately similar according to both the regression (15.7 kN/m) and simultaneous (16.2 kN/m) methods. However, the average $GA_{eff}$ values estimated by the simultaneous method were 3.3% higher. Nevertheless, the simultaneous method yielded an average reduction of 6.75% in $GA_{eff}$ values for two-layer beams.

(5) As the distance from the supports towards the center of the beam increases, the bending stress values also increase. Furthermore, the bending stress values displayed a comparable pattern in both the two-layer beams with span-to-height proportions of 6 and 30, as well as in the single-layer beams. Contrary to the varying bending stress values, the shear stress values were discovered to be consistent across the entire length of the beam.

(6) At a span-to-height proportion of 6 to 18 for two-layer specimens, the beam failed due to tension splitting at the bottom layer. This failure occurred at the midspan of the beam and did not involve any separation of the layers. The main factors leading to the failure of beams with a span-to-height proportion ranging from 18 to 30, were tensile stress in the bottom layer and substantial delamination.

## CRediT authorship contribution statement

**Hojat Hematabadi:** Conceptualization, Methodology, Formal analysis, Investigation, Data Curation, Writing - Original Draft, Writing - Review & Editing, Visualization. **Adefemi A Alade:** Methodology, Investigation. **Robert H. R. Carne:** Methodology, Investigation. **Milinda Yapa:** Methodology, Investigation. **Armando G. McDonald:** Conceptualization, Resources, Writing - Review & Editing, Supervision, Project administration, Funding acquisition. **Daniel Robertson**: Conceptualization, Methodology, Data Curation, Writing - Original Draft, Writing - Review & Editing, Supervision, Project administration, Funding acquisition. **Ahmed A. Ibrahim:** Conceptualization, Methodology, Writing – Original Draft, Writing - Review & Editing, Supervision, Project administration, Funding acquisition

## Conflicts of Interest

There are no conflicts of interests.

## References:

[1] Altıparmak SC, Xiao B. A market assessment of additive manufacturing potential for the aerospace industry. J Manuf Process 2021; 68: 728–38. https://doi.org/10.1016/j.jmapro.2021.05.072.

[2] Karimzadeh M, Basvoju D, Vakanski A, Charit I, Xu F, Zhang X. Machine Learning for additive manufacturing of functionally graded materials. Materials 2024, 17, 3673 https://doi.org/10.3390/ma17153673.

[3] Paolini A, Kollmannsberger S, Rank E. Additive manufacturing in construction: A review on processes, applications, and digital planning methods. Additive Manufacturing 2019; 30: 100894. https://doi.org/10.1016/j.addma.2019.100894.

[4] Altıparmak SC, Yardley VA, Shi Z, Lin J. Extrusion-based additive manufacturing technologies: State of the art and future perspectives. Journal of Manufacturing Processes 2022; 83: 607–36. https://doi.org/10.1016/j.jmapro.2022.09.032.

[5] Rane K, Strano M. A comprehensive review of extrusion-based additive manufacturing processes for rapid production of metallic and ceramic parts. Advances in Manufacturing 2019; 7: 155–73. https://doi.org/10.1007/s40436-019-00253-6.

[6] Tu H, Wei Z, Bahrami A, Ben Kahla N, Ahmad A, Özkılıç YO. Recent advancements and future trends in 3D concrete printing using waste materials. Developments in the Built Environment 2023; 16. https://doi.org/10.1016/j.dibe.2023.100187.

[7] Xin F, Liu W, Song L, Li Y. Research of Compound Additives on Moisture Resistance of Sand Cores Bonded by Sodium Silicate. International Journal of Metalcasting 2023; 17: 753–60. https://doi.org/10.1007/s40962-022-00805-w.

[8] Baiano A. 3D Printed Foods: A Comprehensive Review on Technologies, Nutritional Rate, Safety, Consumer Attitude, Regulatory Framework, and Economic and Sustainability Issues. Food Reviews International 2022;

38: 986–1016. https://doi.org/10.1080/87559129.2020.1762091.
[9] Nurhudan AI, Supriadi S, Whulanza Y, Saragih AS. Additive manufacturing of metallic based on extrusion process: A review. Journal of Manufacturing Processes 2021; 66: 228–37. https://doi.org/10.1016/j.jmapro.2021.04.018.
[10] Sta. Agueda JRH, Chen Q, Maalihan RD, Ren J, da Silva ÍGM, Dugos NP, et al. 3D printing of biomedically relevant polymer materials and biocompatibility. MRS Communications 2021; 11:197–212. https://doi.org/10.1557/s43579-021-00038-8.
[11] Mishra T, Mandal P, Rout AK, Sahoo D. A state-of-the-art review on potential applications of natural fiber-reinforced polymer composite filled with inorganic nanoparticle. Composites Part C: Open Access 2022; 9: 100298.https: //doi.org/10.1016/j.jcomc.2022.100298.
[12] Mustapha KB, Metwalli KM. A review of fused deposition modelling for 3D printing of smart polymeric materials and composites. European Polymer Journal 2021; 156:110591. https://doi.org/10.1016/j.eurpolymj.2021.110591.
[13] Zhang D, Liu X, Qiu J. 3D printing of glass by additive manufacturing techniques: a review. Frontiers of Optoelectronics 2021; 14:263–77. https://doi.org/10.1007/s12200-020-1009-z.
[14] Alhumayani H, Gomaa M, Soebarto V, Jabi W. Environmental assessment of large-scale 3D printing in construction: A comparative study between cob and concrete. Journal of Cleaner Production 2020; 270:122463. https://doi.org/10.1016/j. jclepro.2020.122463.
[15] Pessoa S, Guimarães AS, Lucas SS, Simões N. 3D printing in the construction industry - A systematic review of the thermal performance in buildings. Renewable and Sustainable Energy Reviews 2021; 141:110794. https://doi.org/10.1016/j. rser.2021.110794.
[16] Li Z, Xing W, Sun J, Feng X. Multiscale structural characteristics and Heat–Moisture properties of 3D printed building Walls: A review. Construction and Building Materials 2023; 365. https://doi.org/10.1016/j.conbuildmat.2022.130102.
[17] Ford S, Despeisse M. Additive manufacturing and sustainability: an exploratory study of the advantages and challenges. Journal of Cleaner Production 2016; 137:1573–87. https://doi.org/10.1016/j.jclepro.2016.04.150.
[18] Zhang J, Wang J, Dong S, Yu X, Han B. A review of the current progress and application of 3D printed concrete. Composites Part A: Applied Science and Manufacturing 2019; 125. https://doi.org/10.1016/j.compositesa.2019.105533.
[19] Gomaa M, Jabi W, Veliz Reyes A, Soebarto V. 3D printing system for earth-based construction: Case study of cob. Automation in Construction 2021; 124:103577. https://doi.org/10.1016/j.autcon.2021.103577.
[20] Oladapo BI, Bowoto OK, Adebiyi VA, Ikumapayi OM. Net zero on 3D printing filament recycling: A sustainable analysis. Science of the Total Environment 2023; 894: 165046. https://doi.org/10.1016/j.scitotenv.2023.165046.
[21] Das AK, Agar DA, Rudolfsson M, Larsson SH. A review on wood powders in 3D printing: processes, properties and potential applications. Journal of Materials Research and Technology 2021; 15: 241–55. https://doi.org/10.1016/j.jmrt.2021. 07.110.
[22] Rosenthal M, Henneberger C, Gutkes A, Bues CT. Liquid Deposition Modeling: a promising approach for 3D printing of wood. European Journal of Wood and Wood Products 2018; 76: 797–9. https://doi.org/10.1007/s00107-017-1274-8.
[23] Tofail SAM, Koumoulos EP, Bandyopadhyay A, Bose S, O'Donoghue L, Charitidis C. Additive manufacturing: scientific and technological challenges, market uptake and opportunities. Materials Today 2018; 21: 22–37. https://doi.org/10.1016/j.mattod.2017.07.001.
[24] Hoque Thakur S, Shi C, Kearney LT, Saadi MASR, Meyer MD, Naskar AK, et al. Three-dimensional printing of wood. Science advances 2024; 10: No.10.https://www.science.org/doi/10.1126/sciadv.adk3250
[25] Kam D, Layani M, BarkaiMinerbi S, Orbaum D, Abrahami BenHarush S, Shoseyov O, et al. Additive Manufacturing of 3D Structures Composed of Wood Materials. Advanced Materials Technologies 2019;4.https://doi.org/10.1002/admt. 201900158.
[26] Le Duigou A, Castro M, Bevan R, Martin N. 3D printing of wood fibre biocomposites: From mechanical to actuation functionality. Materials & Design 2016; 96: 106–114. https://doi.org/10.1016/j.matdes.2016.02.018.
[27] Krapež Tomec D, Kariž M. Use of Wood in Additive Manufacturing: Review and Future Prospects. Polymers (Basel) 2022; 14: 1174. https://doi.org/10.3390/polym14061174.
[28] Kariz M, Sernek M, Obućina M, Kuzman MK. Effect of wood content in FDM filament on properties of 3D printed parts. Materials Today Communications 2018; 14: 135–40. https://doi.org/10.1016/j.mtcomm.2017.12.016.
[29] Orji BO, Thie C, Baker K, Maughan MR, McDonald AG. Wood fiber - sodium silicate mixtures for additive manufacturing of composite materials. European Journal of Wood and Wood Products 2023; 81: 45–58. https://doi.org/ 10.1007/s00107-022-01861-z.
[30] Carne RHR, Alade AA, Orji BO, Ibrahim A, McDonald AG, Maughan MR. A screw extrusion-based system

for additive manufacturing of wood: Sodium silicate thermoset composites. Advances in Mechanical Engineering 2023; 15. https://doi.org/10.1177/16878132231210373.
[31] Standard Test Methods of Static Tests of Lumber in Structural Sizes, ASTM D198–15. ASTM International, 2015, https://doi.org/10.1520/D0198-15.
[32] J. Bodig and B. A. Jayne, Mechanics of Wood and Wood Composites. Krieger Pub. 1982. https://api.semanticscholar.org/CorpusID:137359655
[33] Hematabadi H, Hindman DP. Comparison of Test Methodologies for Computing Bending and Shear Stiffness of Cross-Laminated Timber. Journal of Testing and Evaluation 2021; 49: 20200121. https://doi.org/10.1520/JTE20200121.
[34] Hindman DP, Bouldin JC. Mechanical Properties of Southern Pine Cross-Laminated Timber. Journal of Materials in Civil Engineering 2015; 27. https://doi.org/10.1061/(ASCE)MT.1943-5533.0001203.
[35] Standard for Performance-Rated Cross-Laminated Timber, ANSI/APA PRG 320, 2019. https://www.apawood.org/ansi-apa-prg-320.
[36] F. Beer, E. Johnston Jr., J. Dewolf, D. Mazurek, Mechanics of Materials, sixth ed., McGraw-Hill Education, 2010.